remote sensing

MDPI

Article

Assessing Vegetation–Hydrothermal Trend Regimes Across Elevation Gradients in Semiarid Mountains via Gaussian Mixture Models in Saudi Arabia

Asma A. Al-Huqail [1], Zubairul Islam [2,*] and Chigozie Edson Utazi [3]

1 Chair of Climate Change, Environmental Development and Vegetation Cover, Department of Botany and Microbiology, College of Science, King Saud University, Riyadh 11451, Saudi Arabia; aalhuqail@ksu.edu.sa
2 Faculty of Environmental Sciences, Hensard University, Toru Orua 561101, Bayelsa, Nigeria
3 WorldPop, School of Geography and Environmental Science, University of Southampton, Southampton SO17 1BJ, UK; c.e.utazi@soton.ac.uk
* Correspondence: zubairul.islam@hensarduniversity.edu.ng

Highlights

What are the main findings?

- A six-component vegetation–hydrothermal trend classification was retained through multi-criteria model assessment, balancing partition reproducibility, near-optimal held-out predictive performance, classification ambiguity, and parsimony. The resulting regimes represent partially overlapping multidimensional patterns in standardized NDVI, NDWI, and LST trend space.
- Vegetation–hydrothermal trend regimes exhibit a pronounced nonlinear altitudinal reorganization, with a greater prevalence of High Relative LST Trend at low elevations, a Mixed Trend State at mid elevations, and a Low Relative NDWI Trend at higher elevations.

What are the implications of the main findings?

- Climate–regime associations vary systematically along elevation gradients, with temperature-related associations being relatively stronger toward elevation extremes and precipitation-related associations being stronger at intermediate elevations.
- The GMM framework provides a probabilistic, uncertainty-aware approach to characterizing multidimensional vegetation–hydrothermal trend patterns and their classification ambiguity in semiarid mountain environments.

Abstract

Vegetation–hydrothermal trend patterns in semiarid mountains are inherently multidimensional across altitudinal gradients, requiring probabilistic frameworks to characterize overlapping vegetation–hydrothermal trend patterns. We develop a Gaussian mixture model (GMM)-based framework to classify vegetation trend regimes from multidimensional trend variables and to characterize their climate–regime associations across elevation gradients in the semiarid Al Baha region, Saudi Arabia. Landsat time-series data (2014–2025) were used to derive trends in the Normalized Difference Vegetation Index (NDVI), normalized difference water index (NDWI), and land surface temperature (LST) using the Mann–Kendall test. These standardized trend variables were integrated within a probabilistic GMM framework, with candidate models evaluated using Bayesian information criterion (BIC), Integrated Completed Likelihood (ICL), classification entropy, resampling-based partition stability, and held-out predictive performance. Although BIC favored the eight-component VVV model, the six-component solution was retained as a

Check for updates

Academic Editor: Hossein M. Rizeei

Received: 8 July 2026
Revised: 27 August 2026
Accepted: 28 August 2026
Published: 1 September 2026

balanced intermediate-complexity representation based on partition reproducibility, near-optimal predictive performance, classification ambiguity, and parsimony. The results reveal a pronounced elevation-dependent reorganization of vegetation–hydrothermal trends, characterized by High Relative LST Trend dominance at low elevations (~44%), Mixed Trend State at mid elevations (~40.8%), and Low Relative NDWI Trend at higher elevations (>48%), with High Relative LST Trend becoming negligible at the highest altitudes. This spatial organization showed a moderate association with elevation (Cramér's V = 0.299; χ^2 = 74,265.54, $p < 0.001$), with statistical significance interpreted cautiously given the large, spatially autocorrelated sample. Climate–regime analysis further reveals that precipitation variability exhibits the strongest association at mid elevations, whereas temperature shows stronger associations at both low- and high-elevation extremes. Cross-sensor comparison with VIIRS showed substantial classification consistency after class-label alignment (overall agreement ≈ 0.76; $\kappa \approx 0.64$). These findings demonstrate systematic variation in vegetation–hydrothermal trend regimes and their climate associations along elevation gradients. The proposed GMM-based framework provides a scalable and uncertainty-aware approach for assessing climate–vegetation associations in semiarid mountain systems and other data-scarce dryland environments.

Keywords: climate variability; vegetation dynamics; elevation gradients; semiarid mountains

1. Introduction

Climate variability is a dominant control on vegetation dynamics in semiarid mountainous environments [1–3], where elevation gradients amplify spatial heterogeneity in hydrothermal conditions [4]. Small changes in temperature and precipitation can trigger disproportionately large ecological responses [5], producing complex patterns of vegetation change regimes. Mountain systems such as the Sarawat range in Southwestern Saudi Arabia exemplify these dynamics [6], encompassing sharp altitudinal contrasts—from arid lowlands to relatively humid high-elevation zones [7]. These contrasts create tightly coupled climate–vegetation interactions that regulate ecosystem productivity and resilience under changing climatic conditions [8].

Remote sensing has significantly advanced the monitoring of vegetation dynamics by providing continuous observations through indices such as the NDVI, NDWI, and land surface temperature (LST) [9], which capture complementary aspects of vegetation greenness, moisture status, and thermal conditions. When analyzed over time, these indicators offer valuable insights into ecosystem responses to climate variability [10–13]. However, most existing studies treat these variables independently, implicitly assuming linear and isolated responses [14–16]. In reality, vegetation dynamics are driven by interactions among multiple hydrothermal factors rather than any single climatic variable, suggesting that ecosystem responses are more appropriately conceptualized as integrated vegetation–hydrothermal trend regimes rather than single-variable trends [17–19].

Numerous studies have examined vegetation dynamics using statistical and machine learning models [20–23]; however, most of these methods focus on prediction or trend detection and do not explicitly resolve the underlying structure of multidimensional ecosystem responses. In this context, probabilistic approaches such as Gaussian mixture models (GMMs) [24], coupled with objective model selection via the Bayesian information criterion (BIC) [25], provide powerful means to characterize vegetation–hydrothermal trend regimes arising from interacting hydrothermal processes. Nevertheless, their application remains limited, especially in semiarid mountainous systems of the Arabian Peninsula, where strong elevation-driven heterogeneity and nonlinear climate–vegetation interactions require more robust analytical frameworks.

The novelty of the present study lies not in clustering itself, but in integrating probabilistic mixture modeling, explicit classification uncertainty, trend-magnitude assessment, elevation-stratified analysis, and cross-sensor consistency assessment into a unified framework for characterizing multidimensional eco-hydrothermal trend patterns.

Accordingly, this study evaluates three hypotheses: (i) the multidimensional NDVI–NDWI–LST trend space can be represented by probabilistic mixture components that may partially overlap; (ii) the prevalence of the resulting descriptive trend categories varies systematically along elevation gradients; and (iii) climate–regime associations differ across elevation bands.

The main aim of this study was to evaluate how vegetation–hydrothermal trend regimes and climate associations vary along elevation gradients in a semiarid mountainous environment. Specifically, the study examined whether the relative NDVI–NDWI–LST trend configurations and their associations with climatic variables vary systematically across elevation bands.

2. Materials and Methods

2.1. Study Area

The study was conducted in the Al Baha region of Southwestern Saudi Arabia, along the Sarawat Mountains (19.5–20.5°N, 41.0–42.5°E) [26]. The region features a highly heterogeneous mountainous landscape with steep escarpments, elevated plateaus, and low-lying plains (Figure 1). The region has mean annual temperatures of 12–23 °C, annual precipitation of 150–200 mm, and relative humidity of 50–70% [27].

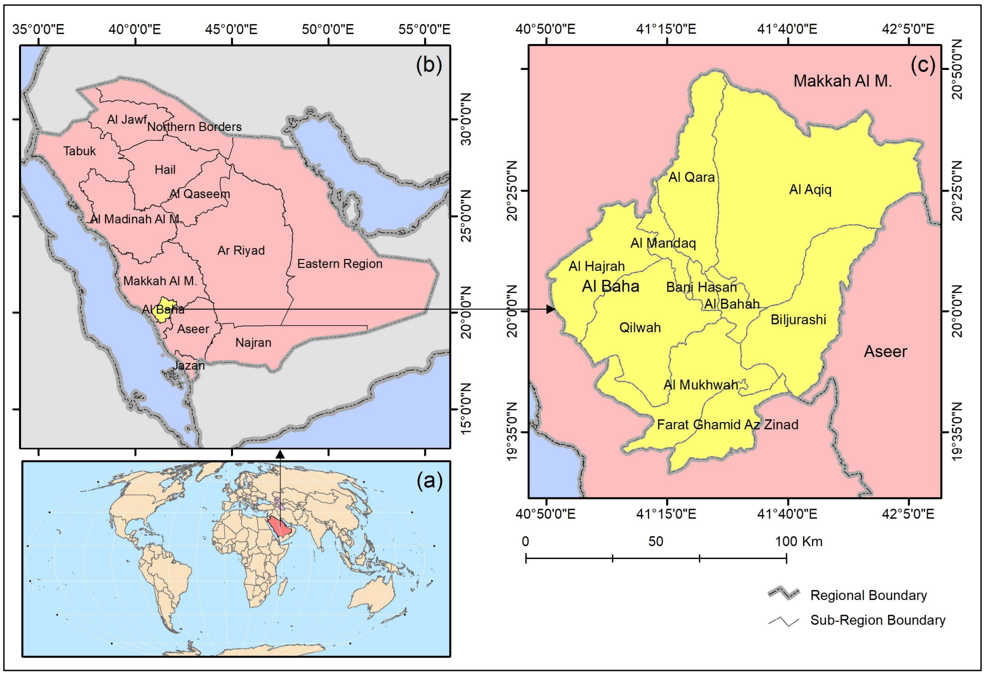

Figure 1. Location map of the study area. (**a**) Global context showing the position of Saudi Arabia. (**b**) National map highlighting the Al Baha region within Southwestern Saudi Arabia. (**c**) Detailed administrative map of the Al Baha region, illustrating sub-regional boundaries.

Elevation bands were adopted to reflect the strong eco-climatic gradients that govern vegetation distribution in Al Baha, where altitude is closely linked to rainfall, temperature, and species composition. These bands capture transitions from arid Tihama plains to humid high-altitude forests, aligning with the observed vegetation zonation and ecological processes (Table 1).

Table 1. Elevation bands adopted for the Al Baha region and their associated eco-climatic and vegetation characteristics reflect altitude-driven gradients in temperature, rainfall, and plant community structure [8] (adapted from Al-Aklabi et al., 2016).

Elevation Band	Range (m)	Characteristics
Low	<300	Arid plains, sparse xerophytes
Lower-mid	300–1000	Wadis, shrubland, moderate moisture
Mid	1000–1800	Transitional, mixed vegetation
High	1800–2100	Woodland, increased rainfall
Very High	>2100	Montane forest, high moisture

Climatically, the region is a semiarid-to-subhumid transition zone influenced by orographic effects. Annual precipitation ranges from ~100 mm in lowland areas to >300 mm at high elevations, with rainfall concentrated during convective events in spring and summer. Temperature regimes also show strong altitudinal variation, with extreme heat in the lowlands and relatively moderate conditions in the highlands.

2.2. Methodological Workflow

Figure 2 summarizes the methodological workflow used to identify vegetation–hydrothermal trend regimes and analyze climate–vegetation associations in the Al Baha region. The framework integrates multi-source remote sensing datasets, including Landsat-derived vegetation and thermal indicators, TerraClimate hydroclimatic variables, VIIRS observations for cross-sensor comparison, and SRTM elevation data, within a harmonized spatiotemporal structure. After preprocessing and trend extraction using the Mann–Kendall approach, standardized NDVI, NDWI, and LST trend variables were integrated into a Gaussian mixture model (GMM) to identify probabilistic vegetation–hydrothermal trend regimes and associated classification uncertainty. The derived regimes were then evaluated across elevation gradients and linked to climate–regime associations using multiple statistical analyses, including MANOVA, ANOVA, likelihood-ratio tests, and random forest importance metrics. This workflow provides a scale-consistent, uncertainty-aware framework for assessing eco-hydrothermal dynamics in semiarid mountain systems.

2.3. Data Sources and Computational Environment

2.3.1. Remote Sensing Data

Vegetation, moisture, and thermal dynamics were derived from Landsat 8 surface reflectance (Collection 2, Level 2) data for 2014–2025 (https://developers.google.com/earth-engine/datasets/catalog/LANDSAT_LC08_C02_T1_L2, accessed on 20 March 2026). A single-sensor approach (Landsat 8 OLI/TIRS) was used to eliminate cross-sensor inconsistencies in multi-platform datasets, thus ensuring radiometric and spectral uniformity across the time series [28].

Landsat observations have a nominal 16-day revisit interval. However, to reduce noise from atmospheric variability and residual cloud contamination, annual median composites were generated for each variable (NDVI, NDWI, and LST). These composites were then used to construct the time series for trend analysis.

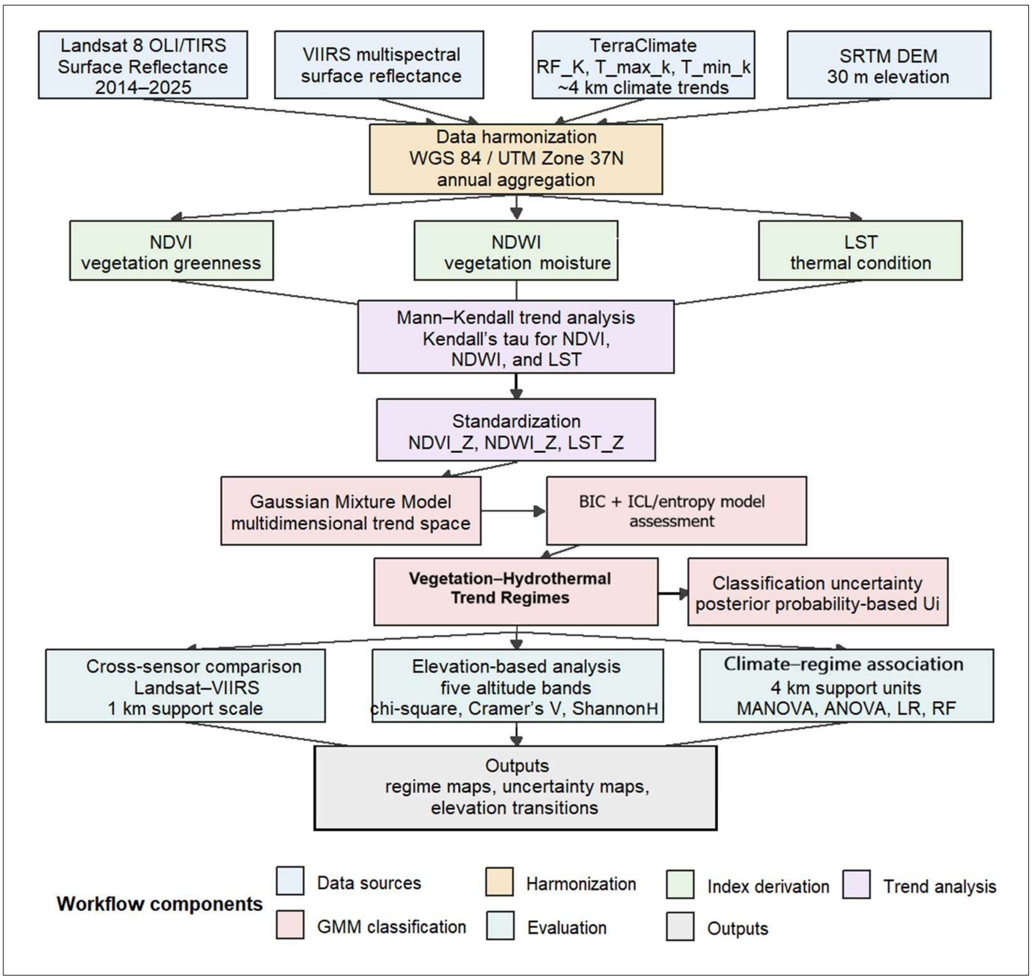

Figure 2. Workflow of the probabilistic eco-hydrothermal trend framework, which integrates Landsat-derived NDVI, NDWI, and LST trends with VIIRS cross-sensor consistency assessment, SRTM elevation bands, and TerraClimate climate variables.

VIIRS observations for cross-sensor consistency assessment were obtained from the Climate Engine platform. Vegetation-related variables were derived from the Suomi National Polar-orbiting Partnership (S-NPP) VIIRS Vegetation Indices Version 2 product (VNP13A1; Earth Engine asset NASA/VIIRS/002/VNP13A1), available in Climate Engine as the VIIRS 500-m 16-day dataset (VIIRS_16DAY). NDVI and the NIR–SWIR1 formulation of NDWI (Gao NDWI; Climate Engine variable NDWI_NIR_SWIR_Gao) were selected to represent vegetation greenness and moisture-related spectral responses, respectively. The VNP13A1 product provides 16-day composites at 500 m spatial resolution using the best available observations within each compositing period [29].

Daytime land surface temperature was obtained separately from the VIIRS Land Surface Temperature and Emissivity daily product (VNP21A1D; Earth Engine asset NASA/VIIRS/002/VNP21A1D), available in Climate Engine as the VIIRS 1-km daily dataset (VIIRS_DAILY). The daytime LST variable (LST_Day_1km) is provided in °C. Both datasets provide coverage throughout the 2014–2025 study period. The 2014–2025 analysis period was specified directly in Climate Engine, and pixel-wise temporal trends were calculated using its Mann–Kendall trend-analysis procedure, with Kendall's Tau-b characterizing the direction and consistency of temporal change. The resulting NDVI, Gao NDWI, and daytime LST trend surfaces were harmonized to a common 1 km spatial resolution for comparison with the Landsat-derived classifications.

2.3.2. Climate Data

Climatic variables, including long-term trend coefficients for precipitation (RF_K), maximum temperature (Tmax, τ), and minimum temperature (Tmin, τ), were obtained from the TerraClimate dataset (https://www.climatologylab.org/terraclimate.html, accessed on 25 March 2026) [30]. TerraClimate provides monthly climate data at ~4 km spatial resolution, which are suitable for long-term hydroclimatic analysis. The TerraClimate archive provides monthly observations for the period 2014–2024; therefore, all climate-related trend analyses were derived from this fully available time series.

2.3.3. Topographic Data

Elevation data were derived from the Shuttle Radar Topography Mission (SRTM) digital elevation model (DEM) at a 30 m spatial resolution (https://developers.google.com/earth-engine/datasets/catalog/USGS_SRTMGL1_003, accessed on 20 March 2026). The DEM was used to classify the study area into elevation bands (low to very high) and to support the analysis of altitudinal variation in vegetation–hydrothermal trend regimes. To ensure spatial consistency, the DEM was resampled and aligned with Landsat-derived datasets in Google Earth Engine (GEE; cloud-based platform).

2.3.4. Data Harmonization

To ensure consistency across multi-source datasets, all variables were harmonized spatially and temporally before analysis. Landsat-derived variables (NDVI, NDWI, and LST), topographic data (DEM), and TerraClimate variables were aligned to a common spatial framework. All datasets were reprojected to a unified coordinate reference system (WGS 84/UTM Zone 37N) and spatially aligned within a common analysis framework. Landsat-derived variables and topographic data were processed at 30 m resolution, whereas TerraClimate variables retained their native effective spatial resolution (~4 km). Resampling was applied solely to facilitate spatial alignment and data integration, and it did not increase the intrinsic spatial detail of the climate data.

Temporal consistency was maintained by aggregating Landsat-derived variables to annual time steps for the period 2014–2025, while TerraClimate-based climate trend analyses were limited to the period 2014–2024 due to data availability. For cross-sensor comparison and climate–regime analysis, Landsat-derived variables were then aggregated to coarser support units (1 km for VIIRS comparison and 4 km for TerraClimate integration), thus matching the effective scale of the auxiliary datasets and minimizing scale mismatch.

The Landsat and TerraClimate periods serve different analytical purposes. The GMM classification was derived independently from the Landsat 2014–2025 record, whereas TerraClimate was used only for the subsequent climate–regime association analysis over the full 2014–2024 period. Availability of an additional TerraClimate year could slightly modify individual climate trend estimates but would not alter the Landsat-derived mixture classification itself. Given the decadal analysis period, the inclusion of 2025 is not expected to fundamentally alter the broad climate–regime association patterns; however, this was not directly tested and is therefore acknowledged as a temporal limitation.

2.3.5. Software and Reproducibility

This study used a Lenovo Legion Pro 5 laptop (Lenovo Group Limited, Beijing, China) with an Intel Core i9-13900HX processor, 32 GB of RAM, and an NVIDIA GPU for computational experiments. All preprocessing and trend analyses were conducted in Google Earth Engine (JavaScript API). Statistical analyses, clustering, and modeling were performed in R (version 4.5.1) using the packages stats (version 4.5.1), mclust (version 6.1.2), randomForest (version 4.7.1.2), and car (version 3.1.3).

https://doi.org/10.3390/rs18172948

All the scripts used in this study are available upon request to ensure reproducibility.

No generative artificial intelligence (GenAI) tools were used for data generation, analysis, or map creation.

2.4. Remote Sensing Processing and Trend Analysis

2.4.1. Data Preprocessing

Landsat imagery was filtered by date and spatial extent. Cloud, shadow, and snow pixels were masked using the QA_PIXEL band [31]. Surface reflectance values were scaled using standard coefficients, and annual median composites were generated to reduce atmospheric noise and residual contamination [32]. Annual median NDVI, NDWI, and LST values were used to characterize long-term eco-hydrothermal conditions and persistent vegetation patterns across elevation gradients. This aggregation emphasizes stable interannual signals relevant to regime identification.

2.4.2. Spectral Indices and Land Surface Temperature

Vegetation greenness and moisture-related spectral responses were quantified using NDVI and the Gao normalized difference water index (Gao NDWI) [33], respectively:

$$NDVI = \frac{NIR - RED}{NIR + RED} \tag{1}$$

$$NDWI = \frac{NIR - SWIR}{NIR + SWIR} \tag{2}$$

where NIR, RED, and SWIR correspond to Landsat bands B5, B4, and B6, respectively. Here, NDWI refers to the Gao NIR–SWIR formulation, also commonly termed NDMI, and is distinct from the green–NIR NDWI used for open-water mapping.

Land surface temperature (LST) was obtained directly from the Landsat 8 Collection 2 Level-2 Surface Temperature product (LANDSAT/LC08/C02/T1_L2) using the ST_B10 band. The Level-2 scale factor and offset were applied as follows:

$$LST_K = (ST\_B10 \times 0.00341802) + 149.0 \tag{3}$$

where LST_K represent surface temperature in Kelvin. LST was subsequently converted to degrees Celsius as $LST_c = LST_K - 273.15$. Because ST_B10 is the Level-2 surface-temperature product, no additional NDVI-based emissivity correction or brightness-temperature retrieval was applied [34].

2.4.3. Trend Detection

Temporal trends were quantified using the nonparametric Mann–Kendall (MK) test [35]:

$$S = \sum_{i=1}^{n-1} \sum_{j=i+1}^{n} \mathrm{sgn}(x_j - x_i) \tag{4}$$

$$Z = \begin{cases} \frac{S-1}{\sqrt{\mathrm{Var}(S)}} & S > 0 \\ 0 & S = 0 \\ \frac{S+1}{\sqrt{\mathrm{Var}(S)}} & S < 0 \end{cases} \tag{5}$$

where n denotes the length of the time series; x_i and x_j represent observations at temporal positions i and $j (j > i)$; and S is the MK test statistic derived from all pairwise comparisons. The sign function $\mathrm{sgn}(\cdot)$ assigns +1, 0, or -1 depending on whether $x_j - x_i$ is positive, zero, or negative, respectively. $\mathrm{Var}(S)$ denotes the variance of S with correction for tied ranks where applicable, and Z is the standardized normal deviate used to evaluate statistical significance.

Because Kendall's τ characterizes the direction and consistency of monotonic association with time rather than the magnitude of change, Sen's slope was also calculated for NDVI, NDWI, and LST. Sen's slope provides the median rate of change per year and was used to characterize trend magnitude within each descriptive regime. For each regime, median Sen's slope and the proportion of observations with statistically significant Mann–Kendall trends ($p < 0.05$) were summarized to distinguish strong, statistically supported trends from weak or non-significant monotonic patterns.

2.4.4. Standardization of Trend Variables

To ensure comparability across variables, the Mann–Kendall trend statistic (Kendall's τ) was standardized using a z-score transformation:

$$Z = \frac{\tau - \mu}{\sigma} \tag{6}$$

where τ denotes the Kendall rank correlation coefficient for each variable, μ is the mean of τ across all spatial units, and σ is the corresponding standard deviation.

The standardized trend variables were subsequently used to characterize vegetation greenness, surface moisture, and thermal conditions for regime classification.

2.5. Vegetation–Hydrothermal Trend Regimes Classification

Gaussian mixture models (GMMs) [36] were fitted to standardized Kendall-τ values for NDVI, NDWI, and LST using the mclust package in R. A probabilistic mixture framework was selected because the multivariate trend space was expected to contain overlapping distributions with unequal covariance structure. Unlike hard-clustering approaches, GMMs estimate posterior component membership probabilities and thereby permit explicit quantification of classification ambiguity.

The multivariate probability density function is defined as follows:

$$f(X_i) = \sum_{g=1}^{G} \pi_g \, \phi(X_i \mid \mu_g, \Sigma_g) \tag{7}$$

where $X_i \in \mathbb{R}^p$ denotes the multivariate feature vector for spatial unit i, comprising the standardized trend variables:

$$X_i = (NDVI_{Z,i}, NDWI_{Z,i}, LST_{Z,i})$$

with $p = 3$ representing vegetation greenness, surface moisture, and thermal conditions, respectively. The parameters π_g, μ_g, and Σ_g correspond to the mixing proportion, mean vector, and covariance matrix of the g-th Gaussian component, where $g = 1, \ldots, G$.

Candidate models with G = 2–8 Gaussian components and various covariance parameterizations were initially assessed using the Bayesian information criterion (BIC) [37]. The VVV covariance structure was then evaluated across G = 2–8 using several complementary model-selection diagnostics. BIC assessed the density model fit, while the Integrated Completed Likelihood (ICL) and classification entropy evaluated component separation and posterior membership ambiguities. As these criteria may support different levels of model complexity, candidate solutions were further assessed using resampling-based partition stability and held-out predictive performance. Partition stability was measured using the Adjusted Rand Index (ARI), considering both agreement between resampled and full-data partitions and pairwise agreement among resampled solutions. Held-out predictive performance was measured using mean test log-density, where higher (less negative) values indicated superior out-of-sample density fit. The final number of components was selected by jointly considering density fit, classification ambiguity, partition reproducibility, predictive performance, and model parsimony, rather than relying on a single diagnostic criterion.

The six resulting vegetation–hydrothermal trend regimes were descriptively labeled High Relative LST Trend, Low Relative NDWI Trend, High NDVI–NDWI Trend, Low Multi-Index Trend, Low Relative NDVI Trend, and Mixed Trend State, according to their relative positions within the standardized NDVI–NDWI–LST trend space. These labels describe dominant relative trend signatures and should not be interpreted as direct measurements of warming, vegetation loss, moisture limitation, physiological stress, or as evidence of discrete ecological state transitions.

Classification uncertainty was quantified as follows:

$$U_i = 1 - \underset{g}{max} P(g \mid X_i) \tag{8}$$

where (P(g | X_i)) denotes the posterior probability of observation (i) belonging to Gaussian component (g). Lower values indicate greater posterior classification confidence, whereas higher values indicate overlap or weak separation among mixture components. This measure represents probabilistic classification ambiguity rather than sensor or measurement error.

2.6. Cross-Sensor Consistency Assessment

For cross-sensor consistency assessment, Landsat-derived vegetation–hydrothermal trend regimes (30 m) were compared with VIIRS-derived trends at a harmonized 1000 m support scale. Landsat classifications were aggregated to 1000 m grid cells using the statistical mode, and regime purity was computed as the proportion of observations belonging to the dominant class. The mode-based aggregation was adopted to provide a single dominant Landsat-derived regime for direct comparison with VIIRS classifications at their native spatial support. Regime purity was used as a complementary metric to quantify within-cell heterogeneity, thereby indicating the extent to which fragmented or mixed vegetation patterns may influence the aggregated classification.

The VIIRS NDVI, NDWI, and LST Kendall trend variables were independently standardized to construct a comparable trend feature space. Unsupervised clustering was applied to derive VIIRS-based regimes, which were ordered according to their relative NDVI–NDWI–LST trend characteristics and aligned with Landsat classes using maximum agreement from cross-tabulated frequencies.

Agreement was evaluated using a confusion matrix, with performance quantified by overall accuracy, Cohen's kappa (κ), balanced accuracy, and class-wise F1 scores.

2.7. Elevation-Based Analysis

Vegetation–hydrothermal trend regimes were analyzed across five elevation bands (low to very high altitudes) to evaluate elevational organization in regime composition. Associations between elevation and regime distributions were assessed using the Pearson chi-square (χ^2) test, Cramér's V effect size, and standardized residuals.

Regime diversity was quantified using Shannon entropy:

$$H' = -\sum p_i ln p_i. \tag{9}$$

https://doi.org/10.3390/rs18172948

2.8. Climate–Regime Associations Analysis

Climate–regime associations were assessed using Kendall trend variables for precipitation, maximum temperature, and minimum temperature derived from TerraClimate data. To address spatial-scale mismatch, regime information from Landsat was aggregated to a 4 km support, which approximately matches the native TerraClimate resolution. For each support unit and elevation band, the dominant regime was determined using the statistical mode, regime purity was retained as an indicator of within-unit heterogeneity, and TerraClimate trend variables were averaged.

Associations were analyzed separately within each elevation band using MANOVA, univariate ANOVA with eta-squared effect size, multinomial logistic regression likelihood-ratio tests, and random forest permutation importance. Each method was interpreted independently, as each quantifies distinct statistical properties. No composite climate-association score was calculated.

A sensitivity analysis was conducted by including continuous elevation as a covariate to account for residual altitudinal variation within broad elevation classes. Baseline models incorporating precipitation, maximum temperature, and minimum temperature trends were compared to elevation-adjusted models using multinomial likelihood-ratio tests, random forest permutation importance, and AIC. This analysis evaluated whether the relative importance and ranking of climate variables remained consistent after accounting for within-band elevation gradients; it was not intended as a formal correction for spatial autocorrelation.

The analysis included 1128 4 km support units, distributed as follows: 139 low, 246 lower-mid, 481 mid, 180 high, and 82 very high. No formal across-band multiplicity correction was applied because the elevation-stratified MANOVA and ANOVA tests were considered separate omnibus analyses rather than a single family of post hoc comparisons. Residual spatial dependence and unequal sample sizes were considered when interpreting the results, with emphasis on effect sizes, sensitivity analyses, and broad spatial patterns.

3. Results

3.1. Vegetation–Hydrothermal Trend Regimes Classification

The BIC comparison identified the eight-component VVV model as the best-supported density solution (Table 2).

Table 2. Multi-criteria comparison of VVV Gaussian mixture models for G = 2–8.

G	BIC	ICL	Mean Entropy	Mean ARI vs. Full	SD ARI	Median ARI	Mean Pairwise ARI	Held-Out Mean Log-Density	Δ Predictive from Best
2	−1,637,800	−1,806,209	0.387	0.465	0.376	0.323	0.458	−3.977	0.090
3	−1,636,612	−1,848,415	0.533	0.357	0.194	0.252	0.372	−3.941	0.055
4	−1,636,325	−1,886,456	0.652	0.353	0.041	0.339	0.546	−3.907	0.021
5	−1,635,351	−1,933,688	0.77	0.359	0.141	0.36	0.405	−3.894	0.007
6	−1,633,959	−1,987,240	0.902	0.479	0.166	0.472	0.408	−3.890	0.004
7	−1,633,809	−1,991,055	0.918	0.462	0.123	0.461	0.408	−3.887	0.001
8	−1,632,762	−2,025,447	1.003	0.445	0.073	0.443	0.433	−3.886	0

Note: G, number of mixture components; BIC, Bayesian Information Criterion; ICL, Integrated Completed Likelihood; ARI, Adjusted Rand Index; SD, standard deviation.

The empirical proportions of the eight components in the BIC-optimal solution were 14.83%, 14.59%, 13.37%, 16.74%, 11.58%, 16.75%, 1.60%, and 10.54%, respectively. As no single value was optimal across all diagnostic criteria, candidate VVV models with G ranging from 2 to 8 were compared using the Integrated Completed Likelihood (ICL), classification entropy, resampling-based stability, and held-out predictive performance. BIC favored G = 8, whereas ICL and entropy increasingly penalized the greater component overlap associated with increasingly complex partitions. The six-component solution demonstrated the strongest agreement with the full-data partition, with the highest mean ARI (0.479) and median ARI (0.472). Held-out predictive performance plateaued by G = 6, with a mean held-out log-density of -3.890 for G = 6 compared to -3.886 for the best-performing G = 8 model, a difference of only 0.004. Therefore, the six-component VVV solution was selected as a balanced, intermediate-complexity representation that combined strong partition reproducibility with near-optimal out-of-sample predictive performance, rather than as the optimum under any single information criterion.

3.1.1. Collinearity of GMM Input Variables

Assessment of the GMM input dimensions indicates limited empirical collinearity. Pearson correlations were 0.399 for NDVI–NDWI, 0.138 for NDVI–LST, and 0.105 for NDWI–LST, while VIF values were 1.203, 1.193, and 1.022 for NDVI, NDWI, and LST, respectively. These results indicate that the three trend dimensions provided largely distinct information within the GMM feature space. Although NDVI, NDWI, and LST may covary environmentally, the observed correlations and VIF values indicate that multicollinearity was limited and unlikely to dominate the estimated GMM covariance structure.

3.1.2. Eco-Hydrothermal Trend Signatures

The descriptive categories occupy distinct relative positions within the standardized NDVI–NDWI–LST Kendall-τ space (Figure 3). Because the standardized values reflect relative monotonic trend positions rather than the magnitude of physical change, the categories are interpreted as comparative trend signatures rather than as absolute states of warming, vegetation loss, or moisture loss.

The High Relative LST Trend category occupies the upper part of the standardized LST trend distribution, whereas the Low Relative NDWI Trend category is characterized primarily by low NDWI monotonic trend values. The High NDVI–NDWI Trend category occupies relatively high positions along both vegetation and moisture dimensions. The Low Multi-Index Trend category is characterized by low vegetation and moisture trend values. The Low Relative NDVI Trend category has low NDVI trend values, and the Mixed Trend State occupies intermediate and overlapping portions of the multivariate feature space.

Sen's slope analysis provided an additional measure of trend magnitude and supported the interpretation of the GMM categories as relative trend configurations. The High NDVI–NDWI Trend category showed the largest median NDVI and NDWI slopes (0.00416 and 0.00299 yr^{-1}), with 86.7% and 69.5% of observations exhibiting statistically significant trends, respectively. In contrast, the Low Relative NDWI Trend category had a substantially smaller median NDWI slope (0.00065 yr^{-1}), with only 5.4% of observations showing a significant trend. The High Relative LST Trend category exhibited a positive median LST Sen's slope, whereas categories with lower relative LST trends showed near-zero or negative slopes, demonstrating consistency between Kendall's τ-based classification and the magnitude and direction of LST change.

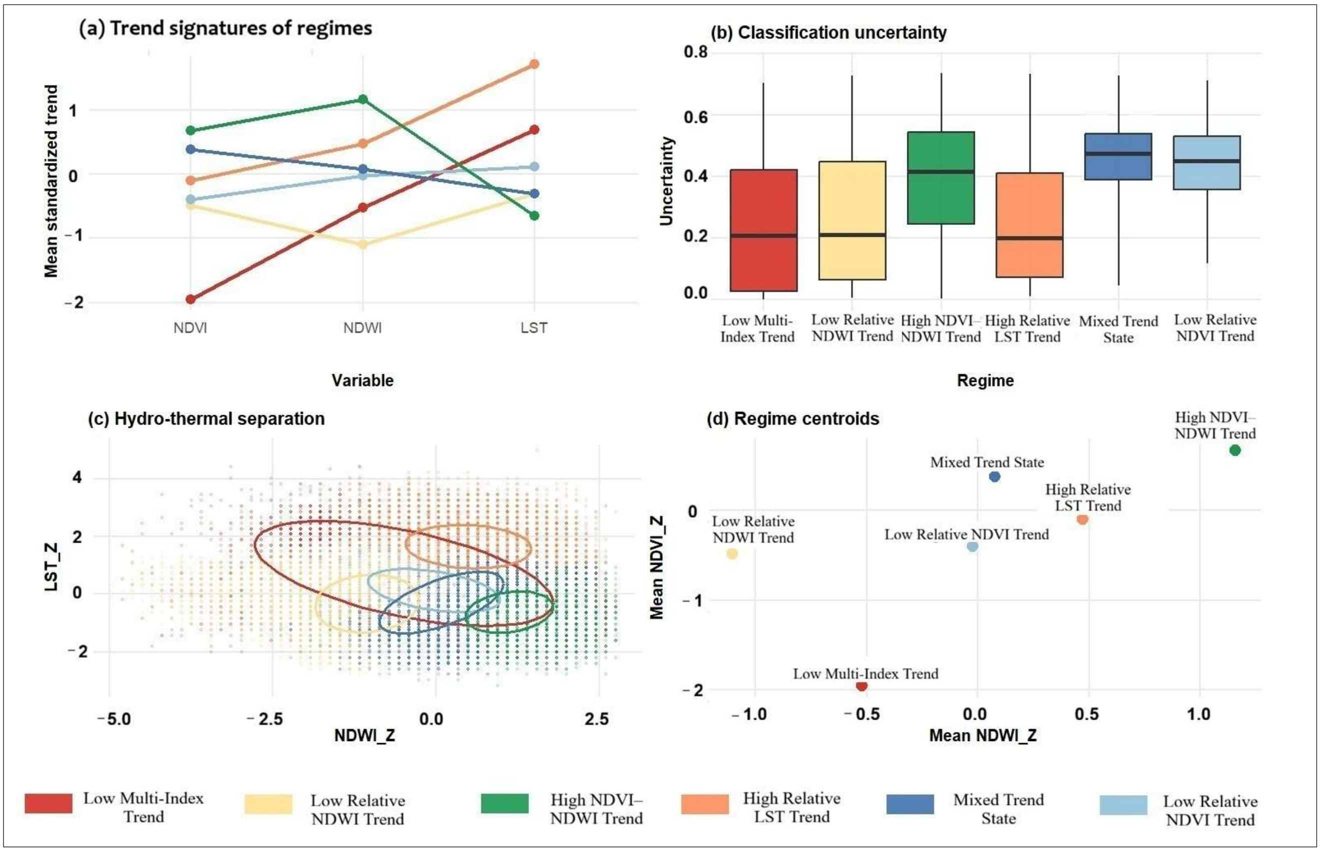

Figure 3. Vegetation–hydrothermal trend regimes and their eco-hydrothermal characteristics across all elevation bands. (**a**) Vegetation–hydrothermal trend signatures. (**b**) Classification uncertainty across regimes. (**c**) Hydrothermal separation in the NDWI–LST space with 68% confidence ellipses. (**d**) Regime centroids in the NDWI–NDVI space.

3.1.3. Uncertainty in Regime Classification

At the regime and elevation levels, classification uncertainty varies systematically across regimes and elevation bands (Figure 4). Mixed Trend State and Low Relative NDVI Trend show the highest uncertainty (median ≈ 0.50–0.55), indicating substantial overlap in hydrothermal conditions and consistency with greater overlap among intermediate trend states within the vegetation–hydrothermal trend continuum. Low Multi-Index Trend and High Relative LST Trend consistently exhibit lower uncertainty, reflecting clearer class separation and greater classification confidence. Low Relative NDWI Trend and High NDVI–NDWI Trend occupy intermediate positions, suggesting partial but organized overlap with adjacent regimes.

Elevation-dependent patterns further reinforce this structure. Uncertainty is highest at lower-mid and mid elevations (median ≈ 0.45–0.50), where multiple trend regimes coexist. Conversely, lower uncertainty at both low and high elevations indicates stronger regime differentiation. High-uncertainty areas, defined as the upper 10% of the uncertainty distribution (UNCERT $\geq$ 0.6166), are concentrated in Mixed Trend regimes and intermediate-elevation zones, corresponding to regions with overlapping temperature and moisture associations. These patterns are consistent with overlap among eco-hydrothermal trend states, although elevated uncertainty may also reflect weak cluster separation, noise in annual composites, or limitations associated with the selected class structure rather than transitions between trend regimes alone.

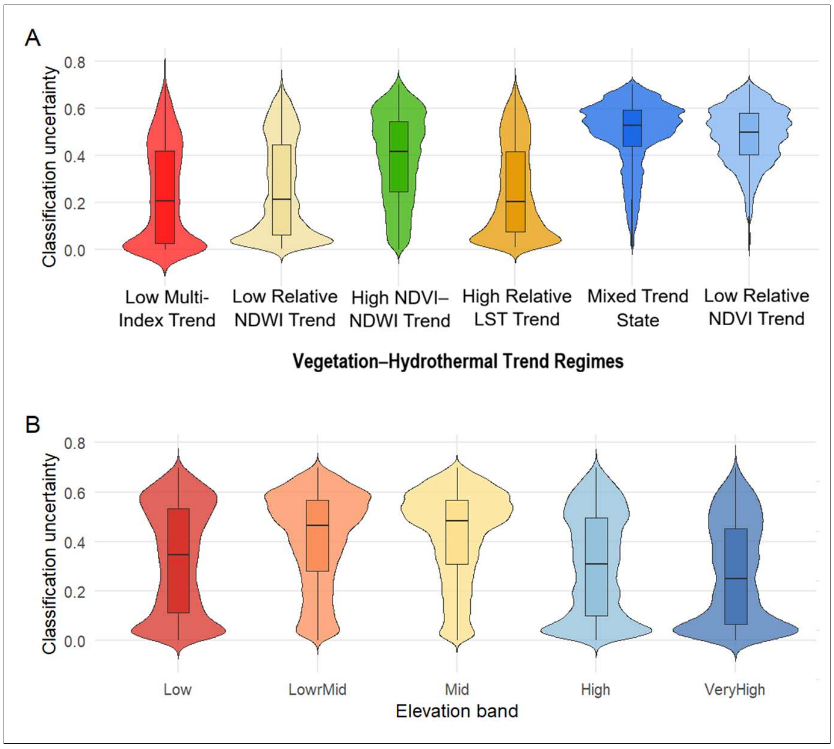

Figure 4. Distribution of GMM classification uncertainty across (**A**) vegetation–hydrothermal trend regimes and (**B**) elevation bands.

3.1.4. Spatial Distribution of Vegetation–Hydrothermal Trend Regimes

The identified regimes exhibit contrasting vegetation–hydrothermal signatures within the standardized NDVI–NDWI–LST trend space. Figure 5 illustrates Low Multi-Index Trend, which covers a limited area of 165.78 km^2 (~1.6%) and is characterized by comparatively low standardized NDVI and NDWI trends, as well as a relatively high LST trend. High Relative LST Trend (1385.54 km^2; ~13.4%) is characterized primarily by a comparatively high standardized LST trend and a relatively weak NDVI trend. Low Relative NDWI Trend (2292.03 km^2; ~22.1%) is distinguished by comparatively low standardized NDWI trends relative to the other dimensions. Low Relative NDVI Trend (1734.26 km^2; ~16.7%) is characterized by comparatively low standardized NDVI trends, with weaker differentiation in the hydrothermal dimensions. Mixed Trend State is the largest mapped category (3272.43 km^2; ~31.6%) and occupies intermediate positions across the NDVI–NDWI–LST trend space. High NDVI–NDWI Trend (1512.11 km^2; ~14.6%) is characterized by comparatively high standardized NDVI and NDWI trends and a relatively lower LST trend. These descriptions represent relative multivariate trend configurations and should not be interpreted as direct evidence of absolute vegetation change, moisture loss or gain, warming, physiological stress, or ecological recovery.

Classification uncertainty quantifies posterior ambiguity rather than providing ecological validation. Overall uncertainty was moderate (mean = 0.3898; median = 0.4443), indicating appreciable overlap among parts of the mixture distribution. These results support structured multidimensional variation in NDVI–NDWI–LST monotonic trends across the study area and indicate that the mixture components represent partially overlapping subdivisions of a continuous multivariate trend space rather than discrete ecological states.

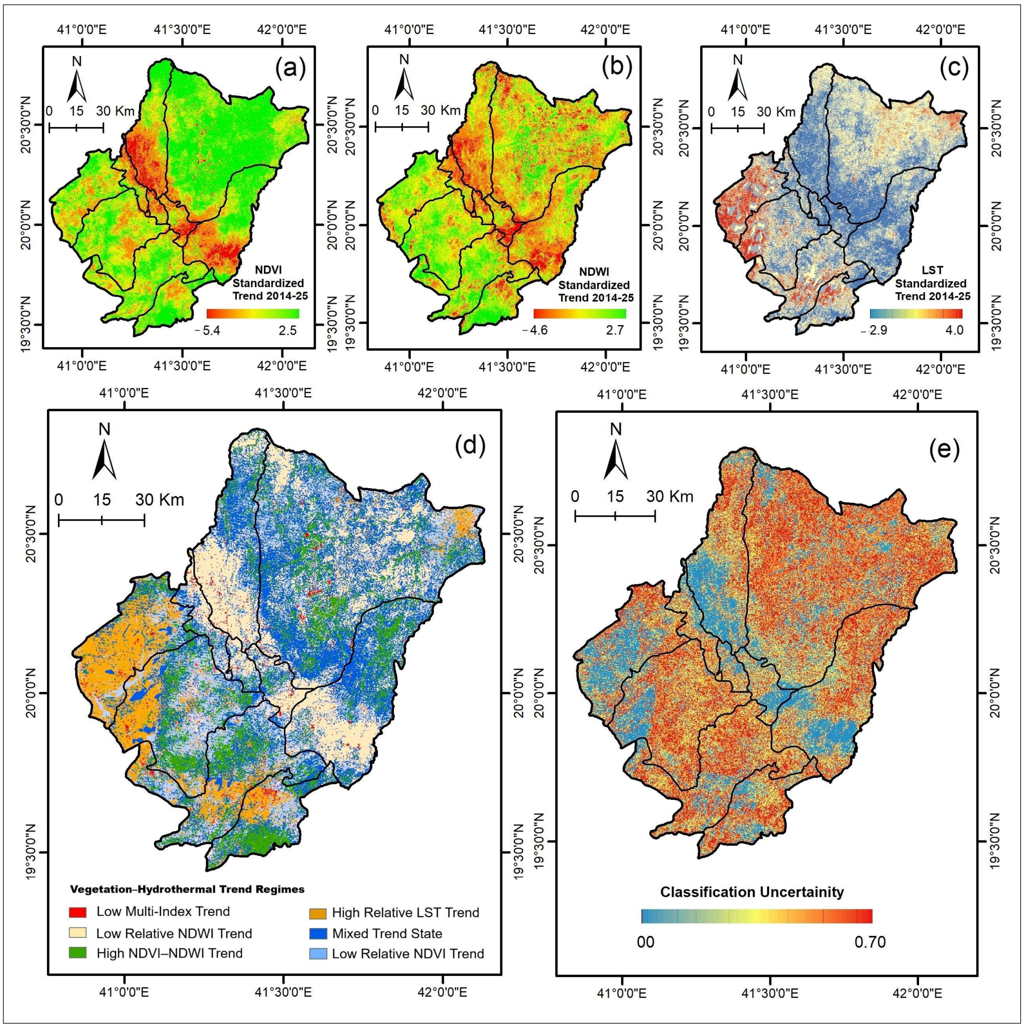

Figure 5. Spatial patterns of vegetation dynamics and derived hydrothermal trend regimes across the Al Baha region (2014–2025). (**a**–**c**) Standardized temporal trends of the NDVI, NDWI, and LST, illustrating spatial heterogeneity in vegetation greenness, moisture status, and thermal conditions; (**d**) resulting vegetation–hydrothermal trend classification and corresponding area distributions (km^2); and (**e**) classification uncertainty.

3.2. Cross-Sensor Consistency Assessment of Vegetation–Hydrothermal Trend Regimes

A cross-sensor comparison of 11,452 harmonized VIIRS support units assessed the consistency between independently derived Landsat and VIIRS trend classifications. Overall agreement was substantial (accuracy = 0.76; κ = 0.64). Because VIIRS classes were independently clustered and then aligned with Landsat classes using maximum cross-tabulated agreement, these statistics quantify cross-sensor consistency after post hoc label matching and do not constitute independent ecological validation.

Mixed Trend State and Low Relative NDWI Trend showed high cross-sensor agreement (F1 score up to 0.82), whereas Low Relative NDVI Trend showed moderate agreement, which reflects greater ambiguity in distinguishing subtle differences in trend characteristics. Misclassification patterns are primarily associated with overlap between Mixed Trend and adjacent regimes, reflecting similarities in their NDVI–NDWI–LST trend characteristics and uncertainty in delineating intermediate trend states.

3.3. Distribution of Vegetation–Hydrothermal Trend Regimes Across Elevation Bands

Regime composition showed pronounced elevational organization (Cramér's V = 0.299). The associated chi-square statistic was large (χ^2 = 74,265.54, p < 0.001); however, given the very large number of spatially autocorrelated observations, statistical significance may be inflated by sample size and spatial dependence, so the *p*-value should not be interpreted as evidence from fully independent samples. Greater emphasis is placed on Cramér's V, mapped spatial patterns, and the relative category composition across elevation bands. At low elevations (1172.11 km^2), the High Relative LST Trend was most prevalent (43.97%; 515.39 km^2), whereas lower-mid elevations showed a more heterogeneous regime composition, with High Relative LST Trend, Mixed Trend State, and Low Relative NDVI Trend occurring in similar proportions (~25% each).

At mid elevations (4807.10 km^2), Mixed Trend State was the most prevalent regime (40.80%; 1961.21 km^2), followed by Low Relative NDWI Trend (25.59%; 1230.10 km^2). The prevalence of High Relative LST Trend declined markedly (2.80%; 134.47 km^2). At higher and very high elevations, Low Relative NDWI Trend accounted for the largest share of mapped regimes (48.38% and 55.37%, respectively), whereas High Relative LST Trend occupied only a very small proportion of the landscape (<1%) (Figure 6).

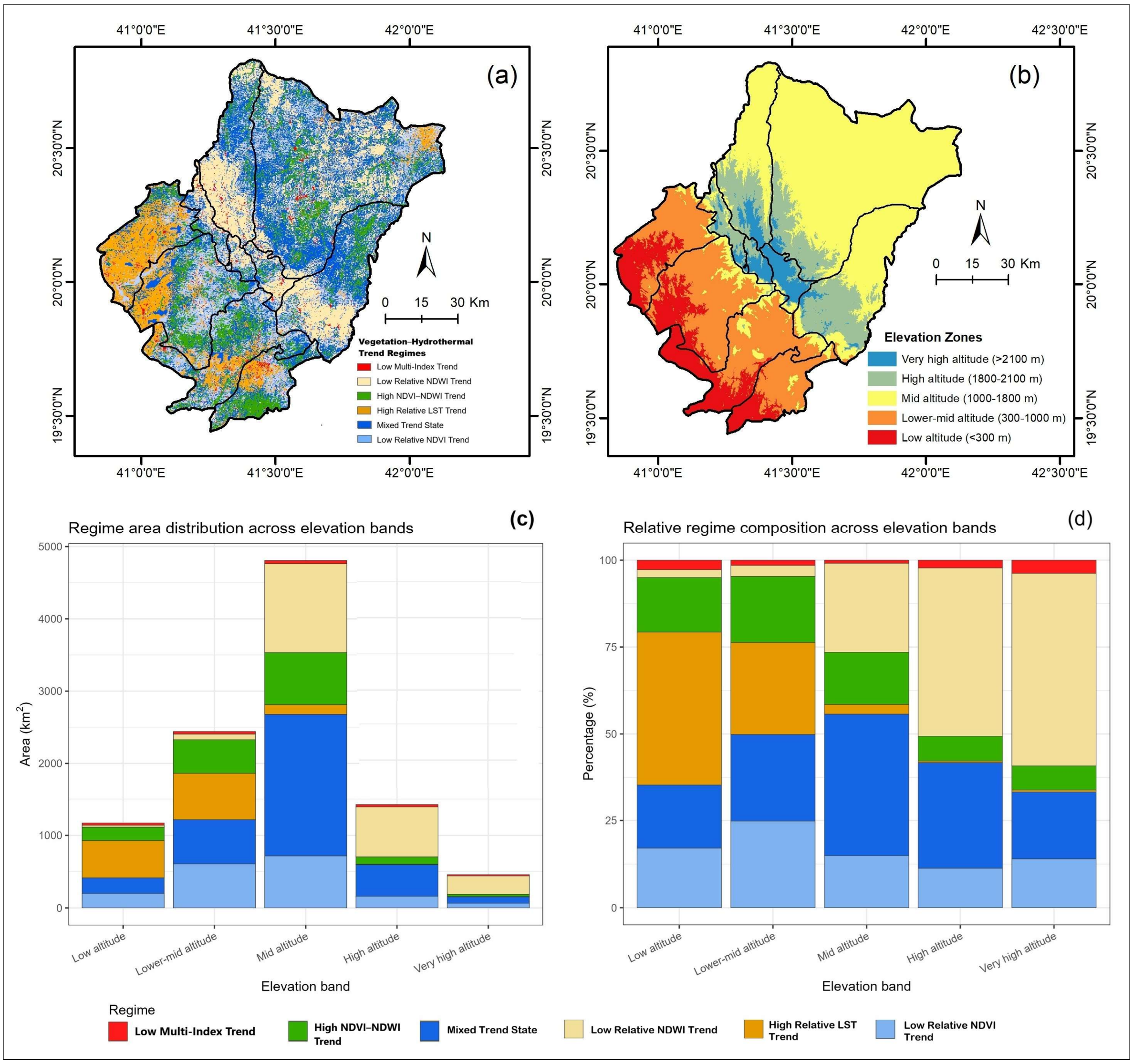

Figure 6. Vegetation–hydrothermal trend regimes in the Al Baha region. (**a**) Spatial distribution of vegetation–hydrothermal trend regimes; (**b**) corresponding elevation zones showing distinct altitudinal bands; (**c**) area distribution (km^2) of vegetation–hydrothermal trend regimes across elevation bands; (**d**) relative regime composition across elevation bands.

Regime diversity follows a nonlinear altitudinal pattern, peaking at lower-mid elevations ($H' = 1.53$) and declining toward higher elevations ($H' \approx 1.26$), which indicates increasing dominance of fewer regimes at elevation extremes.

Standardized residual analysis further confirmed strong elevation-specific associations, with High Relative LST Trends overrepresented at low elevations and Low Relative NDWI Trends strongly concentrated at higher elevations. Mixed Trend States dominate at intermediate altitudes, reflecting intermediate elevation zones.

These results support Hypothesis (ii), demonstrating systematic variation in vegetation–hydrothermal trend regimes along elevation gradients. The observed pattern reveals a structured elevational transition from a greater prevalence of High Relative LST Trends at low elevations to a greater prevalence of Low Relative NDWI Trends at relatively high elevations.

3.4. Climate Associations with Vegetation–Hydrothermal Trend Regimes Across Elevation Bands

Climate–regime associations varied across elevation bands. The analysis used 139 low-, 246 lower-mid-, 481 mid-, 180 high-, and 82 very-high-elevation, 4 km support units. MANOVA indicated multivariate differences among trend categories from low through high elevation, whereas the very-high-elevation result was not statistically significant. Because the very-high-elevation stratum contained the fewest support units ($n = 82$), this non-significant result may partly reflect lower statistical power and should not be interpreted as definitive evidence of reduced climatic differentiation. The spatial patterns of these climatic trends, along with the vegetation change regime, are illustrated in Figure 7.

Climate–regime associations exhibited elevation-dependent patterns in the multivariate and univariate analyses. MANOVA results indicated significant differences in climatic conditions among regimes across low- to high-elevation bands (Wilks' $\lambda = 0.397$–0.723, $p < 10^{-9}$), whereas no significant multivariate separation was observed at very high elevations ($p > 0.05$), indicating no detectable multivariate differentiation within the very-high-elevation stratum.

Univariate ANOVA indicated that climate–regime associations varied across elevation bands. At low elevations, minimum temperature and precipitation showed the strongest associations with regime variation ($\eta^2 = 0.486$ and 0.421, respectively), whereas maximum temperature showed a smaller association ($\eta^2 = 0.054$). At lower-mid and mid elevations, precipitation showed the strongest association (η^2 up to 0.209), and both temperature variables also exhibited associations of varying magnitude. At high elevations, minimum temperature showed the strongest association ($\eta^2 = 0.158$), while the precipitation association was weaker. At very high elevations, maximum temperature showed the strongest observed association ($\eta^2 = 0.127$), although climate–regime associations were generally weaker in this elevation band.

Multinomial likelihood-ratio and random forest permutation-importance analyses showed broadly similar elevation-dependent patterns. Precipitation exhibited the largest likelihood contribution at intermediate elevations, whereas temperature variables showed relatively stronger associations toward the elevation extremes. Random forest permutation importance also showed variation with elevation. Minimum temperature ranked highest at low and high elevations, whereas precipitation ranked highest at lower-mid, mid, and very-high elevations. These measures are interpreted separately because they quantify different statistical properties and are not combined into a composite score.

Sensitivity analysis incorporating continuous elevation as an additional covariate indicated that residual within-band elevation structure contributed to climate–regime differentiation but did not eliminate the broader climate associations. Including elevation improved multinomial model fit across all elevation bands, with ΔAIC values of -4.68, -46.32, -50.29, -27.35, and -1.80 for low, lower-mid, mid, high, and very-high elevations, respectively. The additional contribution of elevation was significant from low through high elevations (likelihood-ratio χ^2 = 12.68–58.29, $p \leq 0.013$), whereas the effect at very high elevation was borderline (χ^2 = 7.80, p = 0.050). Random forest permutation importance retained the same dominant climate variable after elevation adjustment in all five bands: minimum temperature at low (relative importance: 0.554 to 0.552) and high elevations (0.418 to 0.364), and precipitation at lower-mid (0.417 to 0.492), mid (0.398 to 0.390), and very-high elevations (0.407 to 0.397). In contrast, multinomial likelihood-ratio rankings were more sensitive to elevation adjustment: precipitation remained dominant at high elevation and maximum temperature at very high elevation, whereas minimum temperature replaced precipitation as the leading variable at lower-mid and mid elevations. Overall, the elevation-dependent climate–regime associations persisted after accounting for continuous elevation, although the relative importance of precipitation and minimum temperature at intermediate elevations was method-dependent.

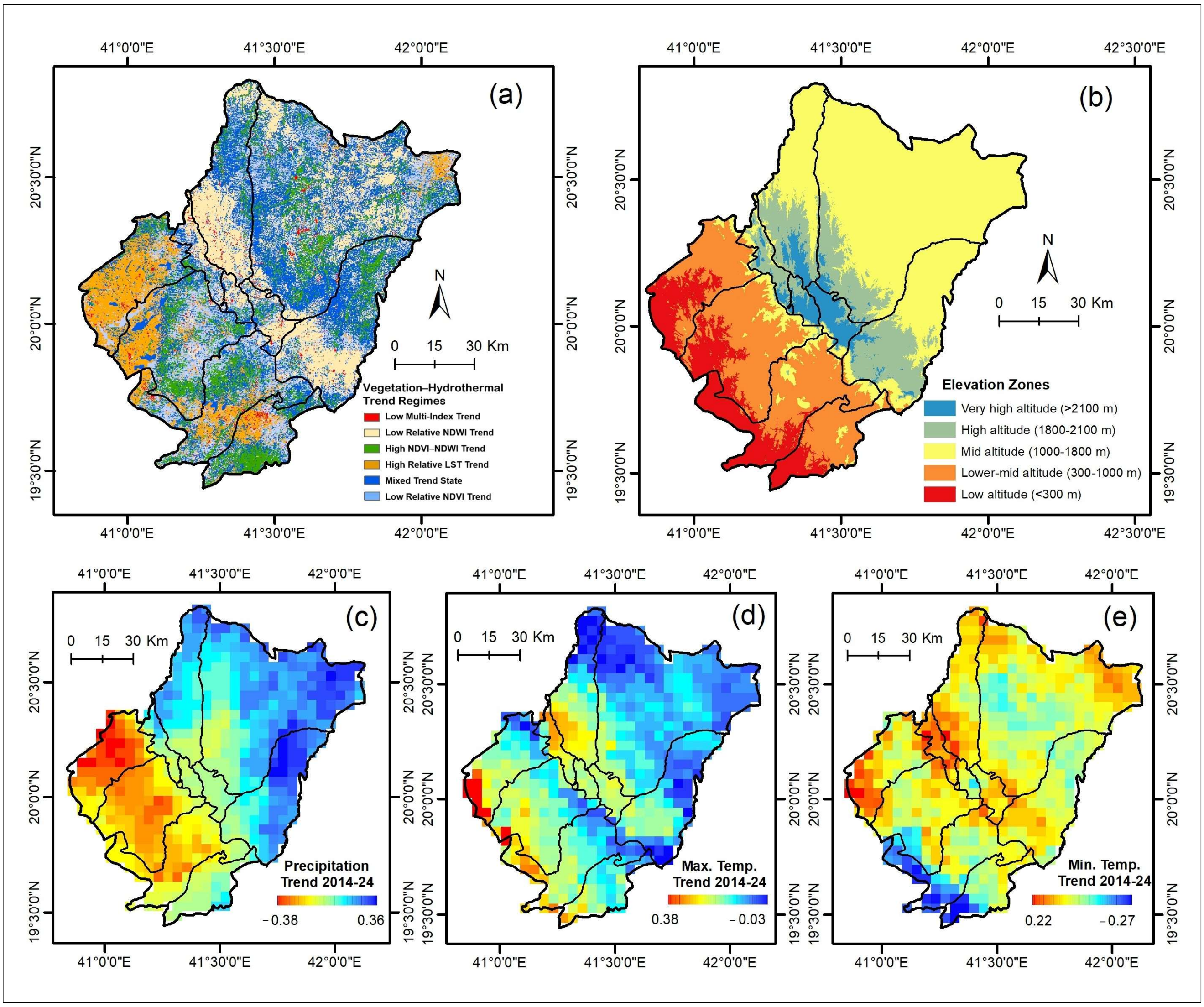

Figure 7. Spatial patterns of (**a**) vegetation–hydrothermal trend regimes, (**b**) elevation zones, and (**c**–**e**) climatic trends (precipitation, and maximum and minimum temperature) for 2014–2024.

Collectively, the analyses demonstrate systematic elevation-related variation in climate–regime associations that persisted after accounting for elevation, although the relative importance of precipitation and temperature at intermediate elevations was method-dependent. These results support Hypothesis (iii) as an elevation-dependent statistical association rather than evidence of direct climatic control. Residual spatial dependence among adjacent 4 km support units nevertheless warrants cautious interpretation.

4. Discussion

4.1. Multidimensional Vegetation–Hydrothermal Trend Regimes in Semiarid Mountains

The probabilistic mixture analysis identifies structured but partially overlapping eco-hydrothermal trend patterns within the NDVI–NDWI–LST feature space. These patterns should not be interpreted as independently validated ecological stress states. Instead, they summarize relative combinations of monotonic vegetation, moisture, and thermal trends, with posterior uncertainty explicitly representing overlap among mixture components.

Sen's slope analysis reinforces this interpretation by demonstrating that relative standardized Kendall-τ positions do not necessarily correspond to absolute vegetation loss, moisture decline, or warming. The descriptive categories, therefore, provide a compact representation of the multidimensional trend structure while retaining the distinction between statistical classification and ecological mechanism.

The identification of six vegetation–hydrothermal trend regimes supports the view that vegetation dynamics in semiarid mountain systems are linked to multiple interacting hydrothermal conditions, as has been widely reported in prior studies [38,39]. The regimes occupy distinct positions within the NDVI–NDWI–LST trend space, confirming that vegetation change is associated with coupled variations in greenness, moisture availability, and thermal conditions [40].

A key contribution of this study is the application of a Gaussian mixture model (GMM) to identify latent eco-hydrothermal regimes within a probabilistic framework. Unlike conventional approaches based on thresholding, k-means clustering, or rule-based classification schemes [41–43], this framework captures both the central tendencies and the overlap among regimes [44], providing a more realistic representation of vegetation–climate associations in heterogeneous terrain. The associated classification uncertainty further reveals that regime boundaries are not fixed but vary spatially [45], with higher uncertainty concentrated in transitional zones where temperature and moisture conditions overlap.

The presence and spatial concentration of Mixed Trend regimes support the interpretation that vegetation dynamics operate along continuous gradients rather than discrete classes. This aligns with ecological theories of gradual regime shifts and resilience [46], which propose that ecosystems respond to climatic variability through progressive reorganization rather than abrupt transitions. In this context, the GMM-based framework not only identifies prevalent eco-hydrothermal trend regimes but also pinpoints areas of elevated uncertainty, offering insight into where eco-hydrothermal trend patterns exhibit greater variability.

4.2. Elevation-Dependent Hydrothermal Associations with Trend Regimes

The altitudinal organization of vegetation–hydrothermal trend regimes indicates an elevation-dependent spatial pattern, although statistical significance should be interpreted cautiously given potential residual spatial autocorrelation. Similar elevation-dependent vegetation responses have been reported, with hydrothermal gradients linked to vegetation productivity patterns and moisture balance under climatic variability [47,48], as well as orographic and topographic effects coinciding with variation in temperature- and moisture-related vegetation dynamics [49].

A pronounced redistribution of prevalent trend regimes is observed along the elevation gradient. Low elevations are characterized by a greater prevalence of the High Relative LST Trend regime, coinciding with positive maximum-temperature trends and negative precipitation trends. At intermediate elevations, the Mixed Trend State becomes more prevalent, with heterogeneous patterns in precipitation and temperature variables. This climatic configuration is consistent with overlapping temperature- and moisture-related associations, rather than being attributable to a single climate variable.

At higher elevations, the Low Relative NDWI Trend regime becomes increasingly prevalent. These areas coincide with negative precipitation trends and positive trends in maximum and minimum temperatures. The co-occurrence of these climatic trends with relatively low NDWI trend signatures indicates a spatial association between hydrothermal trend patterns and climate variability; however, this does not establish a direct climatic or physiological mechanism.

Along the elevation gradient, category prevalence shifts systematically from relatively high LST trend signatures at lower elevations to mixed multivariate signatures at intermediate elevations and to relatively low NDWI trend signatures at higher elevations. These patterns reflect spatial associations among elevation, climate trends, and remotely sensed vegetation–hydrothermal trend configurations, rather than direct evidence of elevation-driven ecological transitions or physiological stress mechanisms.

4.3. Implications for Landscape-Scale Eco-Hydrothermal Patterns

The mapped categories provide a spatially explicit summary of where different combinations of vegetation, moisture, and thermal monotonic trends are most prevalent across the Al Baha landscape. Their principal value lies in identifying areas with contrasting multivariate trend configurations and differing levels of classification uncertainty.

Intermediate elevations contain a comparatively heterogeneous mixture of trend categories and higher posterior uncertainty, which indicates greater overlap among multivariate trend signatures. These areas may therefore warrant closer monitoring in future work, but the present analysis does not establish physiological vulnerability, ecological thresholds, or imminent state transitions.

At both higher and lower elevations, the relative prevalence of particular trend configurations coincides with contrasting climate trends. These relationships provide hypotheses for subsequent process-based or field investigation rather than direct evidence of causal climatic mechanisms.

4.4. Strengths, Limitations, and Sources of Uncertainty

This study integrates multi-source remote sensing data, probabilistic classification, and multi-method statistical analysis within a scale-consistent framework to assess vegetation–hydrothermal trend regimes and their climate–regime associations. A major strength is the application of Gaussian mixture models (GMMs) to multidimensional trend variables, which enables identification of latent eco-hydrothermal regimes and explicit quantification of classification uncertainty. The use of 4 km climate-support units and cross-sensor comparison with VIIRS provide an additional assessment of the reproducibility of broad eco-hydrothermal trend patterns across sensors operating at different spatial resolutions.

Several limitations should be acknowledged. First, the Mann–Kendall approach captures monotonic trends but may overlook abrupt or nonlinear vegetation responses. Consequently, pixels affected by short-term disturbances, such as flash droughts, heatwaves, or rapid recovery events, may show trend signatures that do not fully reflect their underlying dynamics, potentially affecting their assignment to GMM-derived regimes. In addition, the analysis was based on annual median NDVI, NDWI, and LST composites derived from a consistent Landsat 8 observation record spanning 2014–2025. While this approach minimizes cross-sensor inconsistencies and supports robust interannual trend estimation, it may smooth seasonal vegetation responses tied to rainfall timing and short-duration climatic extremes. Therefore, the identified regimes should be interpreted as eco-hydrothermal trend patterns rather than representations of seasonal vegetation dynamics.

Second, the Landsat and TerraClimate analyses cover slightly different periods. The GMM classification is based on Landsat observations from 2014 to 2025, whereas climate–regime associations use the full TerraClimate record for 2014–2024. An additional TerraClimate year could modify individual climate trend coefficients and association estimates, but it would not alter the Landsat-derived mixture classification itself.

Third, aggregating to 4 km climate-support units reduces spatial-scale mismatch but does not render neighboring observations statistically independent. Both climate trends and mapped categories retain strong geographic and elevational structure, so residual spatial autocorrelation may inflate conventional significance statistics. This limitation is particularly relevant to pixel-level elevation–regime tests. Accordingly, effect sizes, mapped proportions, and broad spatial patterns are emphasized over p-values alone. The very-high-elevation climate analysis also has the smallest sample of 4 km support units (n = 82), which may reduce statistical power.

Fourth, the GMM partition was sensitive to the inclusion of NDVI. Although empirical collinearity among NDVI, NDWI, and LST trend variables was low (Pearson NDVI–LST $r = 0.138$; Spearman $\rho = 0.137$; VIF = 1.02–1.20), an NDVI-exclusion sensitivity analysis produced a substantially different partition (ARI = 0.273) and greater classification uncertainty. This indicates that NDVI contributes materially to the multivariate feature space and that cluster stability was not maintained when this dimension was removed. Accordingly, the six-regime solution should be interpreted as conditional on the full three-variable NDVI–NDWI–LST representation, rather than as invariant to feature exclusion.

Finally, NDVI, NDWI, and LST are remotely sensed proxies rather than direct measurements of plant physiological stress, root-zone soil moisture, ecosystem vulnerability, or ecological state transitions. The absence of in situ observations, therefore, precludes direct ecological validation of the mapped trend categories.

4.5. Future Research Directions

Future work should integrate higher-resolution or downscaled climate data, soil moisture observations, evapotranspiration, phenological information, and targeted field measurements to evaluate whether the remotely sensed trend categories correspond to measurable ecological processes.

5. Conclusions

This study characterizes multidimensional vegetation–hydrothermal trend structure along elevation gradients in the Al Baha region using a probabilistic Gaussian mixture framework. BIC favored the eight-component VVV model, while increasing model complexity was accompanied by greater classification entropy and stronger ICL penalization. Considering partition reproducibility, held-out predictive performance, classification ambiguity, and parsimony jointly, the six-component VVV model was retained as a balanced, intermediate-complexity solution for classification and spatial interpretation. The resulting regimes represent relative combinations of monotonic trends in NDVI, NDWI, and LST.

The prevalence of these trend categories varied systematically with elevation, and climate–regime associations also differed across elevation bands. Precipitation showed relatively stronger associations at intermediate elevations, whereas temperature-related variables showed stronger associations at the extremes of elevation. Cross-sensor comparison with VIIRS indicated consistency in broad spatial trend patterns. By explicitly retaining posterior uncertainty and distinguishing between the monotonic trend direction and the Sen slope magnitude, the framework provides a transparent approach to characterizing multidimensional remotely sensed vegetation, moisture, and thermal trends in semiarid mountain environments.

Author Contributions: A.A.A.-H.: Conceptualization, project administration, methodology, writing—original draft, writing—review and editing, funding acquisition. Z.I.: Data curation, formal analysis, methodology, software, writing—original draft, investigation, resources, writing—review and editing. C.E.U.: Methodology, software, visualization, writing—review and editing. All authors have read and agreed to the published version of the manuscript.

Funding: This work was supported by King Saud University, Riyadh, Saudi Arabia, through the Ongoing Research Funding program—Research Chairs (ORF-RC-2026-28-04).

Data Availability Statement: The data used in this study are publicly available. Landsat 8 surface reflectance (Collection 2, Level 2) data were accessed on 20 March 2026 via the Google Earth Engine. TerraClimate climate datasets were accessed on 25 March 2026 from https://www.climatologylab.org/terraclimate.html. The VIIRS-derived products were accessed on 25 March 2026 from the Climate Engine platform (https://app.climateengine.org/climateEngine). The processed datasets and analysis code supporting the findings of this study are available from the corresponding author upon reasonable request.

Acknowledgments: The authors are grateful to King Saud University, Riyadh, Saudi Arabia, for supporting this research through the Ongoing Research Funding program—Research Chairs (ORF-RC-2026-28-04).

Conflicts of Interest: The authors declare that they have no conflicts of interest.

Abbreviations

The following abbreviations are used in this manuscript.

NDVI	Normalized Difference Vegetation Index
NDWI	Normalized Difference Water Index
LST	Land Surface Temperature
GMM	Gaussian Mixture Model
BIC	Bayesian Information Criterion
MK	Mann–Kendall Test
RF	Random Forest
MANOVA	Multivariate Analysis of Variance
ICL	Integrated Completed Likelihood
ARI	Adjusted Rand Index
AIC	Akaike Information Criterion
VIF	Variance Inflation Factor

References

1. Holleman, C.; Rembold, F.; Crespo, O.; Conti, V. *Climate Extremes and Their Impacts on Agriculture and Food Security*; FAO: Rome, Italy, 2020; 108p. [CrossRef]
2. Liu, L.; Gou, X.; Wang, X.; Yang, M.; Qie, L.; Pang, G.; Wei, S.; Zhang, F.; Li, Y.; Wang, Q.; et al. Relationship between extreme climate and vegetation in arid and semi-arid mountains in China: A case study of the Qilian Mountains. *Agric. For. Meteorol.* **2024**, *348*, 109938. [CrossRef]
3. Bastos, A.; Naipal, V.; Ahlström, A.; MacBean, N.; Smith, W.K.; Poulter, B. Semiarid Ecosystems. In *Balancing Greenhouse Gas Budgets*; Elsevier: Amsterdam, The Netherlands, 2022; pp. 311–335. [CrossRef]
4. Measho, S.; Chen, B.; Trisurat, Y.; Pellikka, P.; Guo, L.; Arunyawat, S.; Tuankrua, V.; Ogbazghi, W.; Yemane, T. Spatio-Temporal Analysis of Vegetation Dynamics as a Response to Climate Variability and Drought Patterns in the Semiarid Region, Eritrea. *Remote Sens.* **2019**, *11*, 724. [CrossRef]
5. Johnson, D.W.; Susfalk, R.B.; Gholz, H.L.; Hanson, P.J. Simulated Effects of Temperature and Precipitation Change in Several Forest Ecosystems. *J. Hydrol.* **2000**, *235*, 183–204. [CrossRef]
6. Ghazanfar, S.A. Biogeography and Conservation in the Arabian Peninsula: A Present Perspective. *Plants* **2024**, *13*, 2091. [CrossRef]

7. UNESCO. World Heritage Centre. Available online: https://whc.unesco.org/en/tentativelists/6640/ (accessed on 18 April 2026).
8. Al-Aklabi, A.; Al-Khulaidi, A.W.; Hussain, A.; Al-Sagheer, N. Main Vegetation Types and Plant Species Diversity along an Altitudinal Gradient of Al Baha Region, Saudi Arabia. *Saudi J. Biol. Sci.* **2016**, *23*, 687–697. [CrossRef]
9. Thepvongsa, J.; Butar Butar, E.S. Analytical Study on the Relationship among Land Surface Temperature, Land Use Land Cover, and Spectral Indices Using Geospatial Techniques over Sikhottabong District, Laos. *Case Stud. Chem. Environ. Eng.* **2025**, *12*, 101269. [CrossRef]
10. Hussien, K.; Kebede, A.; Mekuriaw, A.; Beza, S.A.; Erena, S.H. Spatiotemporal Trends of NDVI and Its Response to Climate Variability in the Abbay River Basin, Ethiopia. *Heliyon* **2023**, *9*, e14113. [CrossRef]
11. Wu, Y.; Yang, J.; Li, S.; Guo, C.; Yang, X.; Xu, Y.; Yue, F.; Peng, H.; Chen, Y.; Gu, L.; et al. NDVI-Based Vegetation Dynamics and Their Responses to Climate Change and Human Activities from 2000 to 2020 in Miaoling Karst Mountain Area, SW China. *Land* **2023**, *12*, 1267. [CrossRef]
12. Lu, Y.; Yu, Y.; Sun, L.; Li, C.; He, J.; Guo, Z.; Duan, L.; Zhang, J.; Yu, R. NDVI Based Vegetation Dynamics and Responses to Climate Change and Human Activities at Xinjiang from 2001 To 2020. *Sci. Rep.* **2025**, *15*, 25848. [CrossRef]
13. Opiyo, S.B.; Pienaar, L.; Piketh, S.J.; Burger, R.P.; Chikoore, H.; Havenga, H. Assessment of Vegetation Density Trends in Response to Long-Term Climate Change Impacts in Western South Africa (1962–2022) Using SPEI and NDVI Time Series. *Discov. For.* **2025**, *1*, 29. [CrossRef]
14. Du, J.; Fu, B.; Guo, Q.; Shi, P. Monitoring and Assessment of the Oasis Ecological Resilience Improved by Rational Water Dispatching Using Multiple Remote Sensing Data: A Case Study of the Heihe River Basin, Silk Road. *Remote Sens.* **2020**, *12*, 2577. [CrossRef]
15. Rahimi, E.; Dong, P.; Jung, C. Global NDVI-LST Correlation: Temporal and Spatial Patterns from 2000 To 2024. *Environments* **2025**, *12*, 67. [CrossRef]
16. Weng, Q.; Lu, D.; Schubring, J. Estimation of Land Surface Temperature–Vegetation Abundance Relationship for Urban Heat Island Studies. *Remote Sens. Environ.* **2004**, *89*, 467–483. [CrossRef]
17. Guo, W.; Shi, H.; Jiao, X.; Huang, W.; Chen, K.; Yue, X.; Yin, S.; Jiang, Y.; Wang, H. Hydrological Responses and Multi-Pathway Regulatory Mechanisms Associated with Vegetation Change in the Yellow River Basin. *Ecol. Indic.* **2026**, *183*, 114686. [CrossRef]
18. Bayazit, E.; Kartal, V.; Sammen, S.S.; Scholz, M. Climate-Induced Vegetation Stress Detected Through Remote Sensing of Hydroclimatic Indicators. *Sustainability* **2026**, *18*, 2235. [CrossRef]
19. Adeyeri, O.E.; Zhou, W.; Ndehedehe, C.E.; Wang, X. Global Vegetation, Moisture, Thermal and Climate Interactions Intensify Compound Extreme Events. *Sci. Total Environ.* **2024**, *912*, 169261. [CrossRef]
20. Abolhasani, A.; Tavili, A.; Khosravi, H. Simulating Different Scenarios of Vegetation Dynamics under the Influence of Human and Climatic Factors Based on the Residual Trend Analysis and Machine Learning. *Sci. Rep.* **2026**, *16*, 6485. [CrossRef]
21. Ma, N.; Cao, S.; Bai, T.; Yang, Z.; Cai, Z.; Sun, W. Assessment of Vegetation Dynamics in Xinjiang Using NDVI Data and Machine Learning Models from 2000 To 2023. *Sustainability* **2025**, *17*, 306. [CrossRef]
22. Wang, Q.; Jiang, S.; Zhu, Y.; Wang, Y.; Han, S.; He, F.; Ma, M.; Zhao, Y. Attribution of Vegetation Dynamics Using an Interpretable Machine Learning Model in the Haihe River Basin, China. *Ecol. Front.* **2025**, *45*, 1135–1146. [CrossRef]
23. Xia, Z.; Liao, K.; Guo, L.; Wang, B.; Huang, H.; Chen, X.; Fang, X.; Zu, K.; Luo, Z.; Shen, F.; et al. Determining Dominant Factors of Vegetation Change with Machine Learning and Multisource Data in the Ganjiang River Basin, China. *Land* **2025**, *14*, 76. [CrossRef]
24. Scrucca, L.; Fop, M.; Murphy, T.B.; Raftery, A. mclust 5: Clustering, Classification and Density Estimation Using Gaussian Finite Mixture Models. *R J.* **2016**, *8*, 289–317. [CrossRef]
25. Mindrila, D. Bayesian Latent Class Analysis: Sample Size, Model Size, and Classification Precision. *Mathematics* **2023**, *11*, 2753. [CrossRef]
26. Alharbi, B.S. Effectiveness of machine learning algorithms for estimating montane vegetation from high-resolution satellites: A case study between Al-Baha and Baljurashi area, Saudi Arabia. *Int. J. Image Data Fusion* **2025**, *16*, 2498349. [CrossRef]
27. Ibrahim, H.M.; Alghamdi, A.G.; Aly, A.A. Assessing Drought Patterns in Al-Baha: Implications for Water Resources and Climate Adaptation. *Sustainability* **2024**, *16*, 9882. [CrossRef]
28. Landsat Collection 2 Surface Reflectance. Available online: https://www.usgs.gov/landsat-missions/landsat-collection-2-surface-reflectance (accessed on 20 March 2026).
29. Visible Infrared Imaging Radiometer Suite | NASA Earthdata. Available online: https://www.earthdata.nasa.gov/data/instruments/viirs (accessed on 25 March 2026).
30. Abatzoglou, J.T.; Dobrowski, S.Z.; Parks, S.A.; Hegewisch, K.C. TerraClimate, a High-Resolution Global Dataset of Monthly Climate and Climatic Water Balance from 1958–2015. *Sci. Data* **2018**, *5*, 170191. [CrossRef]
31. Hughes, M.J.; Kennedy, R. High-Quality Cloud Masking of Landsat 8 Imagery Using Convolutional Neural Networks. *Remote Sens.* **2019**, *11*, 2591. [CrossRef]
32. Zhao, P.; Lu, D.; Wang, G.; Wu, C.; Huang, Y.; Yu, S. Examining Spectral Reflectance Saturation in Landsat Imagery and Corresponding Solutions to Improve Forest Aboveground Biomass Estimation. *Remote Sens.* **2016**, *8*, 469. [CrossRef]

33. Ashok, A.; Rani, H.P.; Jayakumar, K.V. Monitoring of Dynamic Wetland Changes Using NDVI and NDWI Based Landsat Imagery. *Remote Sens. Appl. Soc. Environ.* **2021**, *23*, 100547. [CrossRef]
34. Earth Resources Observation and Science (EROS) Center. *Landsat 8–9 Operational Land Imager/Thermal Infrared Sensor Level-2, Collection 2*; U.S. Geological Survey: Reston, VA, USA, 2020. [CrossRef]
35. Yue, S.; Pilon, P.; Cavadias, G. Power of the Mann–Kendall and Spearman's Rho Tests for Detecting Monotonic Trends in Hydrological Series. *J. Hydrol.* **2002**, *259*, 254–271. [CrossRef]
36. Garcia-Dias, R.; Vieira, S.; Lopez Pinaya, W.H.; Mechelli, A. Clustering Analysis. *Mach. Learn.* **2020**, 227–247. [CrossRef]
37. Konishi, S.; Kitagawa, G. Bayesian Information Criteria. In *Information Criteria and Statistical Modeling*; Springer: New York, NY, USA, 2007; pp. 211–237. [CrossRef]
38. Han, X.; Lei, S.; Yang, Y.; Tian, Y.; Xu, Y.; Chen, H.; Guo, Y. Hydrothermal Coordination Dominated Vegetation Restoration in Open-Pit Mine Reclamation across Multiple Climatic Zones in Arid and Semi-Arid China. *J. Environ. Manag.* **2025**, *394*, 127440. [CrossRef]
39. Ge, X.; Ding, J.; Amantai, N.; Xiong, J.; Wang, J. Responses of Vegetation Cover to Hydro-Climatic Variations in Bosten Lake Watershed, NW China. *Front. Plant Sci.* **2024**, *15*, 1323445. [CrossRef]
40. Na, R.; Na, L.; Du, H.; He, H.S.; Shan, Y.; Zong, S.; Huang, L.; Yang, Y.; Wu, Z. Vegetation Greenness Variations and Response to Climate Change in the Arid and Semi-Arid Transition Zone of the Mongo-Lian Plateau during 1982–2015. *Remote Sens.* **2021**, *13*, 4066. [CrossRef]
41. Moussaid, A.; Bayad, M.; Gamoussi, Y.; El Hamdouni, Y.; Briak, H. K-Means Clustering Applied to Vegetation Indices for Mapping Cultivated Areas Using High-Resolution Moroccan Mohammed VI Satellite Imagery. *Sci. Rep.* **2026**, *16*, 11040. [CrossRef]
42. Wen, L.; Ryan, S.; Powell, M.; Ling, J.E. From Clusters to Communities: Enhancing Wetland Vegetation Mapping Using Unsupervised and Supervised Synergy. *Remote Sens.* **2025**, *17*, 2279. [CrossRef]
43. Niu, Y.; Zhang, H.; Han, W.; Zhang, L.; Chen, H. A Fixed-Threshold Method for Estimating Fractional Vegetation Cover of Maize under Different Levels of Water Stress. *Remote Sens.* **2021**, *13*, 1009. [CrossRef]
44. Viroli, C.; McLachlan, G. Deep Gaussian mixture models. *Stat. Comput.* **2017**, *29*, 43–51. [CrossRef]
45. Ye, X.; Zhou, W. Unsupervised Classification of Global Temperature Profiles Based on Gaussian Mixture Models. *J. Mar. Sci. Eng.* **2025**, *13*, 92. [CrossRef]
46. Bel, G.; Hagberg, A.; Meron, E. Gradual regime shifts in spatially extended ecosystems. *Theor. Ecol.* **2012**, *5*, 591–604. [CrossRef]
47. Körner, C. The use of 'altitude' in ecological research. *Trends Ecol. Evol.* **2007**, *22*, 569–574. [CrossRef]
48. Pepin, N.; Bradley, R.S.; Diaz, H.F.; Baraer, M.; Caceres, E.B.; Forsythe, N.; Fowler, H.; Greenwood, G.; Hashmi, M.Z.; Liu, X.D.; et al. Elevation-dependent warming in mountain regions of the world. *Nat. Clim. Change* **2015**, *5*, 424–430. [CrossRef]
49. Scherrer, D.; Körner, C. Topographically controlled thermal-habitat differentiation buffers alpine plant diversity against climate warming. *J. Biogeogr.* **2011**, *38*, 406–416. [CrossRef]